Research Article
Vol. 27, No. 9 | 29 Apr 2019 | OPTICS EXPRESS 13400
Optics EXPRESS

Development of a modular, high-speed plenoptic-camera for 3D flow-measurement

ZU PUAYEN TAN,[1,2] KYLE JOHNSON,[1] CHRIS CLIFFORD,[1] AND BRIAN S. THUROW[1,3]

[1] *Advanced Flow Diagnostics Lab, Department of Aerospace Engineering, Auburn University, 211 Davis Hall, Auburn, AL 36849, USA*
[2] *zzt0012@auburn.edu*
[3] *thurow@auburn.edu*

Abstract: This paper describes the development of a Modular Plenoptic Adaptor (MPA) for rapid and reversible conversion of high-speed cameras into plenoptic imaging systems, with the primary goal of enabling single-camera, time-resolved 3D flow-measurements. The MPA consists of a regular imaging lens, a microlens array, a tilt-adjustable microlens mount and an optical relay, which are collectively installed onto a high-speed camera through a standard lens mount. Each component within the system is swappable to optimize for specific imaging applications. In this study, multiple configurations of the MPA were tested and they demonstrated the ability to refocus and shift perspectives within high-speed scenes after capture. Additionally, the MPA demonstrated 3D reconstruction of captured scenes with <1% spatial error across a volume spanning approximately $50\times30\times50mm^3$. Finally, the MPA also demonstrated reconstruction of a 3D droplets-field with sufficient quality to support qualitatively accurate plenoptic particle image velocimetry (PPIV) calculations.

1. Introduction

Light-field (LF) imaging has enjoyed rapid growth in recent years [1], owing to increasingly powerful camera sensors and computational tools. Modern applications that benefit from LF imaging include, but are not limited to: post-capture refocusing and perspective-shifting in photography [2], occlusion-detection and depth-estimation [3], machine-vision [4,5] and fluid flow-measurements [6–18]. The study reported in this paper focuses on extending LF imaging capabilities to high-speed videography with the primary interest of application for time-resolved, 3D flow-measurements.

As a motivator, most practical flow-fields exhibit highly three-dimensional (3D) and unsteady structures. The majority of modern 3D flow measurement techniques are based on tomography, where the same measurement volume is imaged from multiple perspectives, and a digital reconstruction of the volume is subsequently performed post-capture. Notable examples of these techniques include: computed-tomography chemiluminescence [19–22], volumetric laser-induced fluorescence [23–27], tomographic BOS [28] and tomographic particle image velocimetry (tomo-PIV) [29–31]. Four perspectives are typically used for tomo-PIV with additional views usually required for scalar-field measurements. While the multi-camera tomographic techniques outlined above have become the standard for 3D flow-measurements, a new wave of research is currently focused on minimizing the number of required image sensors and/or viewpoints in order to (i) reduce system cost, (ii) reduce setup complexity, and (iii) enable 3D measurements in facilities with very limited optical-access (e.g., high-pressure combustion rigs, supersonic tunnels or shock-tubes). Notable techniques that have been developed include employing a scanning laser-sheet [32], holography [33], structured-light illumination [34,35], and fiber-optics-based or mirror-based view-splitting for single/dual-camera tomography [36,37].

#361260
Journal © 2019
https://doi.org/10.1364/OE.27.013400
Received 5 Mar 2019; revised 12 Apr 2019; accepted 12 Apr 2019; published 25 Apr 2019

In recent years, our group at Auburn University has explored the use of a LF imaging device called the plenoptic camera to perform single/dual-camera 3D flow-measurements. The plenoptic camera was originally popularized by Adelson & Wang [38], Levoy et al. [39,40], Lumsdaine & Georgiev [41], Wu et al. [42] and Ng et al. [2] for post-capture refocusing and range-finding. As shown on the left of Fig. 1, the plenoptic camera is a special case of LF imaging where the scene's 4D LF (having spatial dimensions s,t and angular dimensions u,v) is captured by a single main lens with a dense microlens array located at its image plane. Each microlens projects the incident rays onto the sensor as a small circular "microlens sub-image," examples of which are shown on the right of Fig. 1. Each sub-image captures a very small span of u,v and s,t, thereby encoding the incident rays' angles (u,v) as spatial information for post-capture sampling. Hence, a large array of microlenses not only captures the subjects' s,t positions, but also their rays' u,v angles, which carries information about the subjects' z depth.

With its depth-capturing capability, plenoptic imaging has been developed into 3D flow-measurement techniques such as plenoptic-PIV (PPIV) [6–11], 3D particle-tracking [12] and 3D BOS [13–15] by our group, as well as 3D thermometry and multi-plane Doppler-based velocimetry by others [16–18]. Critically, these techniques demonstrated that 3D flow-fields can be measured by a single plenoptic camera. Furthermore, these techniques are generally also able to measure a deeper volume than traditional tomography due to plenoptic camera's refocusing capability. A variation of our existing plenoptic camera is shown in Fig. 2, while details of its development can be found in [6,9]. The system consists of an Imperx Bobcat low-speed camera (both 16 and 29MP variants). Since the microlens array's image plane has to coincide with the sensor in this canonical "Plenoptic 1.0" design, the array has to be located at one microlens focal length away from the sensor ($\mathcal{O}$ (0.1-1)mm). Thus, conversion of the Imperx camera into plenoptic camera requires removal of the protective glass in front of its sensor as well as removal of any obstructing camera housing material. Final integration of the microlens array into the camera involves attaching a three-piece array-bracket around the sensor. Micro adjustment screws have been incorporated into the bracket to allow for precise tilt alignment. Although the resulting system is compact, microlens installation/removal is laborious and risks sensor damage. The system frame rate is limited by the image sensor to approximately 4 fps and also is incapable of UV laser-induced fluorescence and other imaging applications where an intensifier/filter is needed between the array and sensor.

Building on past works, this paper describes a new study whose objective is to develop a high-speed ($\geq 1kHz$) light-field imaging system that is compatible with the cost and functional constraints of high-speed cameras, with the intent of using the system for time-resolved, plenoptic flow-measurements. The presented results will demonstrate the developed system's capability at (i) allowing rapid and reversible conversion between regular and plenoptic imaging, (ii) recording high-quality plenoptic images, (iii) refocusing/reconstruction a 3D scene with <1% spatial error, (iv) filming a slow-motion footage of high-speed scene for post-capture refocusing/perspective-shift, (v) plenoptic imaging through an intensifier and (v) volumetrically reconstructing a droplets-field to sufficient quality for PPIV to be performed.

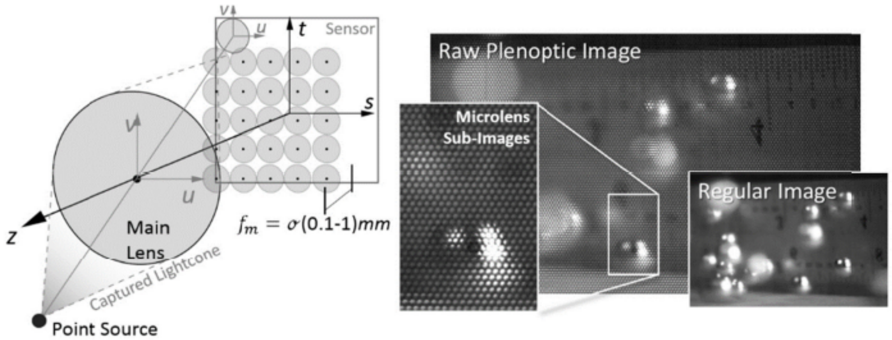

Fig. 1. *Left*: Optical configuration of a plenoptic camera. *Right*: Comparison of a traditional camera's image with a raw plenoptic image, which shows the grid of microlens sub-images.

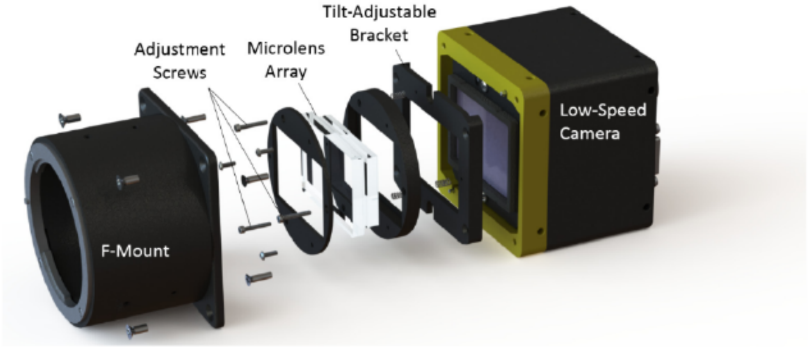

Fig. 2. Plenoptic camera developed by Auburn University. Further details [6,9].

2. Methodology: development of the high-speed plenoptic system

2.1 Design constraints and approach to high-speed plenoptic imaging

A high-speed plenoptic imaging system has several unique design constraints:

a. Cost and risk: Due to high-speed cameras' high costs, the plenoptic conversion process should avoid permanent modifications to the camera (including removal of the protective glass to install an on-sensor microlens array).

b. 3D/2D flexibility: Plenoptic imaging sacrifices spatial resolution in order to encode angular information in the image. Thus, the high-speed plenoptic system should be easily back-convertible to 2D, high-resolution imaging when 3D is not required.

c. Resolution and speed balance: Since 1 microlens approximately equates to 1 final image pixel, and each microlens typically ≥ 8 pixels in diameter to sufficiently resolve angles, the chosen high-speed camera should correctly balance speed and resolution based on the final image requirements. Cameras with very different pixel pitches may also require different sets of microlens array.

d. Add-ons flexibility: High-speed imaging often requires optical add-ons such as an intensifier, especially for laser-induced fluorescence and chemiluminescence measurements. Since angular information of the light rays is lost through an intensifier, the microlens array has to be placed before the intensifier to pre-encode ray angles as spatial information.

However, as part of Fig. 3 shows, an intensifier's imaging plane (its photocathode) is typically situated behind an inlet window having $<$ (1)mm thickness, which exceeds the microlens' focal length. Thus, direct placement of the microlens array on top of the intensifier is not possible.

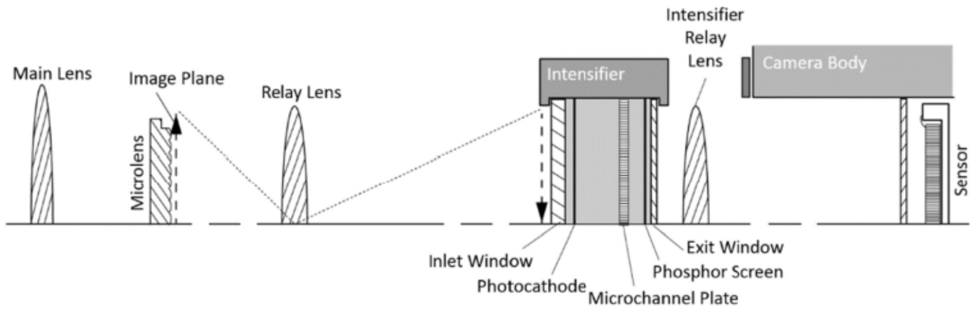

Fig. 3. General configuration of a relayed plenoptic system for an intensified high-speed camera.

Due to these constraints, an embedded on-sensor microlens array (as was used in our previous work; Fig. 2) would no longer be feasible. Instead, the approach of an externally-attached modular plenoptic adaptor (MPA) was chosen. Key challenge for implementing an MPA involves breaking the traditional < (0.1-1)*mm* distance constraint between the microlens array and imaging-plane. Inspired by the design of camera intensifier where a relay lens is often used to project the phosphor screen's image onto the sensor, Fig. 3 shows that a similar approach can be applied to plenoptic imaging where the microlens array's image-plane is projected through relay onto the recording plane. Since conventional relay lens' image plane is approximately 46.5*mm* aft of the lens' rearmost element (i.e., if common F-mount camera lenses are used) compared to the microlens' < (0.1-1)*mm*, a significant length of unobstructed space is created around the relayed image plane using this approach.

Five notable precedents of relayed plenoptic cameras exist. The first was designed by Adelson & Wang [38] for range-finding. They described a system where the microlens image plane is relayed by a lens to the sensor array. Few details were provided regarding the relay design except the use of a Nikon 60*mm* macro lens. To counter vignette generated by the relay system, they employed both a field lens to straighten the rays entering the microlens array, as well as a ground-glass diffuser on the back of the array to homogenize the angles of exiting rays at the expense of signal-to-noise ratio.

A later work by Drazic et al. [43] used the relay lens concept to develop plenoptic video-camera for broadcast. For their application, the microlens sub-images had to be perfectly-aligned with the sensor's pixels, because inter-pixel interpolation was computationally-prohibitive for broadcast. Drazic et al. [43] did not succeed in their development because the relay lenses introduced too much distortion for exact microlens-to-pixel alignment (a requirement that does not apply to 3D flow-characterization).

In 2015 Fischer et al. [18] succeeded in constructing a relayed plenoptic system for an ultra high-speed camera (49*kHz*). However, their application was focused on performing droplets/particles Doppler velocimetry across multiple discrete planes (2 planes demonstrated), and the low-resolution microlens array employed (25x25 microlenses at 0.25*mm* each) does not support practical imaging purposes.

One of the most recent works on relayed plenoptic was reported by Dansereau et al. [5], who employed relay lens during the prototyping phase of their monocentric-lens wide-FOV plenoptic camera. Their prototype contained a microlens array extracted from the Lytro Illum LF camera (1/2" form-factor), while the relay system consisted of a microscope objective that directly images the array, followed by a Sigma 85*mm* f/1.4 lens to telecenterize the rays. Another pair of 85*mm* and microscope lenses arranged symmetrically behind the first pair then relays the image onto the sensor. A 1:1 relay is thus achieved with low aberrations.

However, this design is inherently very long (a total of four relay lenses) and suitable to smaller sensors (~4*mm* in the cited paper).

A similarly recent work by Liu et al. [44] showed a system developed for 3D flame-imaging. Notably, their design used an optical-cage system to rigidly confine all optical elements to a common optical axis. Two Nikon 50*mm* f/1.8D lenses mounted front-to-front were used for 1:1 relay, with the proposition that the second lens will serve to cancel the distortions introduced by the first lens. Liu et al. [44] reported success in being able to isolate chemiluminescence from different depth planes within two overlapping Bunsen burner flames.

2.2 Detailed design of the Modular Plenoptic Adaptor (MPA)

Detailed design of our MPA is shown in Fig. 4. The design evolved outwards using the microlens array as the key constraint. Unlike many previous works [5,18,43,44] that likely employed microlens arrays sized for smaller format sensors (either explicitly described or inferred from their microlens housing's dimensions), we chose to employ a 35*mm* full-frame format microlens-array. This allows the array to be backwards-compatible with most high-resolution, low-speed cameras, which typically use the full-frame format. Cross-camera compatibility is thus maximized to reduce the costs of fabricating multiple microlens arrays.

Inspired by Liu et al's [44]'s work, the MPA uses an off-the-shelf Thorlab 60*mm* optical-cage system to rigidly constrain the main lens, microlens and relay lens on the same optical axis. The cage unit consisted of two cage-plates on its ends with standard F-mount adaptors. Distance between the plates can be adjusted to accommodate relay lenses of different focal distances, which made the system largely lens-agnostic. The microlens array was mounted on a sled in the middle of the unit. The back of the relay lens interfaced directly with the high-speed camera, while the cage-plates also contained optical-post mounting points for the device. The developed MPA can be attached to or detached from a high-speed camera within minutes like a standard lens, compared to traditional on-sensor microlens mounting techniques that require camera disassembly in a cleanroom.

It was observed during tests that minor flexing/sagging can occur along the system during setup despite the cage system's rigidity, which may upset the microlens and sensor's parallel alignment. Thus, the final MPA design incorporated a microlens holder which floated on three spring-loaded tilt adjustment screws to allow further fine-tuning after the system is mounted, similar to our existing design in Fig. 2. This is in addition to a z-axis micro-translation stage that allows the array to be placed exactly at the relay lens' focal-plane. xy-translations were not incorporated as their alignment was not crucial. A 3D-printed housing slides around the cage to protect the microlens array and relay lens from dust and stray reflections.

Finally, the MPA employed a Tamron 60*mm* f/2 macro lens for relay during our tests. As reported by Drazic et al. [43] and Liu et al. [44], lens distortion is a critical challenge when relaying a plenoptic image, since any distortion becomes large compared to the scale of the microlens. In particular, Drazic et al. [43] suggested that field-curvature from the relay lens can cause a loss of "plenopticity" if the spherical relay lens focal-plane and flat microlens image-plane are significantly misaligned. Both authors have used a twin-lens relay design to minimize distortions. However, our tests revealed that a single Tamron lens was able to produce a high quality relayed image (as Section 3.1 will show) because macro lenses are optimized from the outset to have a low field-curvature on close-up subjects. Furthermore, the Tamron lens naturally provides a 1:1 magnification at its closest focal distance and employs internal focusing, which greatly simplifies setup and adjustment of the MPA.

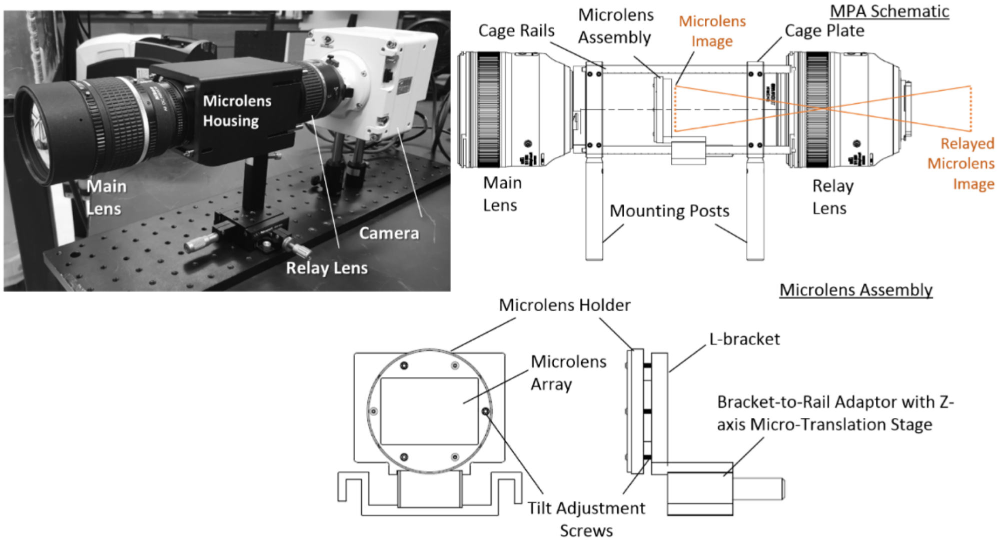

Fig. 4. Schematic and photo of the developed MPA connected to a high-speed camera.

3. Results and discussions

Four proof-of-concept tests were conducted for the MPA/high-speed camera system: (i) the sensor, microlens array and main lens were mutually calibrated to characterize the quality of relay; (ii) a spatial-calibration dot-plate was imaged at known depths and their images reconstructed in 3D to characterize the system's spatial accuracy; (iii) scenes were filmed with and without intensifier to demonstrate post-capture refocusing and perspective-shift; and (iv) time-resolved, 3D tomographic reconstruction, as well as PPIV, were performed on a recorded scene of flowing droplet particles. These experiments and their results are described below:

3.1 Test 1: relay quality

As shown in Fig. 1, a raw plenoptic image consists of a grid of microlens sub-images. Exact coordinates of each sub-image's center must be known in order to correctly sample the image during refocusing/perspective-shift/tomographic reconstruction. A common method of coordinates-determination involves narrowing the main lens aperture, which consequently narrows the sub-images down to dots, where each dot represents the corresponding microlens' exact center [7]. The left of Fig. 5 shows a microlens centers calibration image taken through the MPA. The zoomed images 1 and 2 show that very tight and uniformly-spaced dots were recorded, indicating that the relayed image was in sharp focus and contains few distortions. Thus, the lens distortion issue that plagued Drazic et al. [43] did not seem to affect our MPA significantly. Zoomed image 3 contains dots that were barely visible, but otherwise uniform, which suggests low distortion but substantial vignette on the edges- an issue that is in line with the reports of Adelson & Wang [38] and Liu et al. [44].

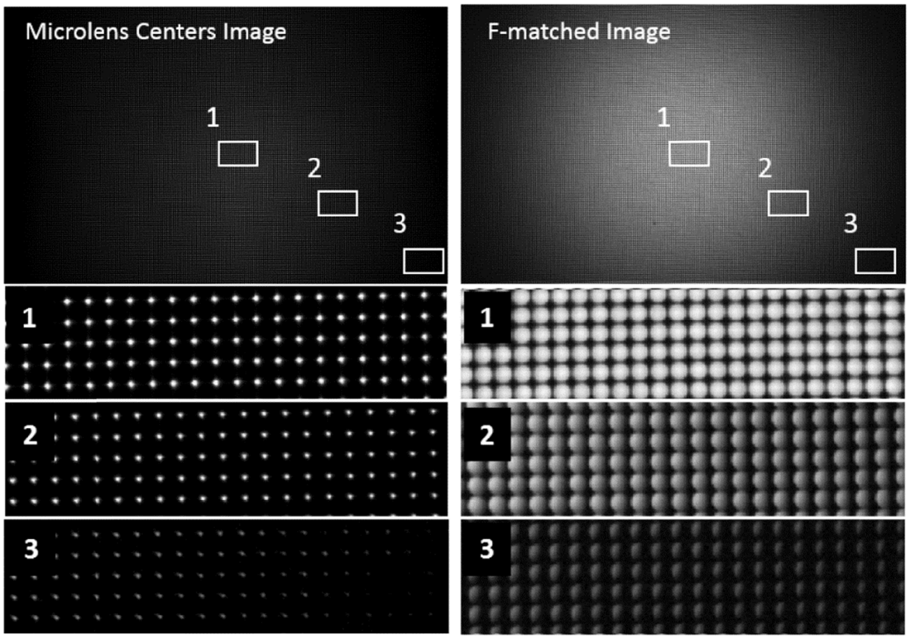

Fig. 5. Quality of the relayed microlens image. *Left*: image of the microlenses' centers. *Right*: image of the microlens sub-images when the main lens F-number is correctly adjusted.

Narrowing the main lens aperture reduces the sub-images' diameter. Conversely, widening the main lens enlarges the sub-images. The correct main lens F-number was set by incrementally opening the aperture until the sub-images' edges were within $1px$ of contacting, as shown on the right of Fig. 5. As before, uniformly spaced sub-images were achieved throughout the relayed image. However, sub-images close to the edge became crescent-shaped as their outer-corners were shaded by vignette.

Base on Fig. 5, the MPA/high-speed camera combination was expected to deliver distortion-free and well-focused image across the entire field. Due to the rays' large angles behind the F/4 microlens, the image is vignetted along the edges where rays could not reach the relay lens' finite front aperture. It was found through first-order model and experimental data, however, that light-loss along the central non-vignetted region is insignificant (i.e., close to the original F/4 microlens). Alternative large-aperture relay lens or a field-lens/diffuser technique [38] may be used to reduce vignette in future work.

3.2 Test 2: reconstruction spatial accuracy

Establishing the MPA/high-speed camera system's measurement accuracy is critical for PPIV and plenoptic tomographic applications. The spatial accuracy of the system's reconstructed volumes was characterized using the same procedure employed by Hall et al. [45] for low-speed plenoptic camera:

1. A metal calibration dot-plate with holes drilled in a regular $5mm$ grid pattern was set up at the MPA's nominal focal plane, parallel to and laterally centered on the sensor.
2. A set of calibration-images were captured with the dot-plate traversed to −25, −20, −15, −10, −5, 0, 5, 10, 15, 20, $25mm$ relative to the nominal focal plane (positive away).
3. A set of test-images were captured with the dot-plate at −23, −13, −3, 3, 13, $23mm$.

4. The calibration-images were used to create a polynomial mapping [45] between object space coordinates and pixels on the camera sensor. This mapping combined plenoptic ray-tracing physics with the physics of perspective warp, magnification and simple lens distortion. The mapping process also tied each voxel in the reconstructed volume to an object space coordinate.
5. The test-images were refocused and de-warped onto their corresponding planes using the polynomial mapping. Matlab's *imfindcircles* was used to identify dots within the reconstructed test-images, and the dots' coordinates were compared to their known ground-truth coordinates.
6. The same procedure was repeated with the dot-plate and its traverse-axis rotated by θ = 20 and 40^o, representing practical multi-camera tomography experiments where multiple cameras would be set some angle apart [11,45]. The axis of rotation intersected the nominal focal-plane as well as the system's optical axis.
7. Three combinations of microlens arrays and high-speed cameras as outlined in Table 1 were tested in order to characterize the effects of microlens pitch and camera pixel resolution on reconstruction accuracy.

A sample result is provided in Fig. 6, the left column of which shows three test-images taken with the dot-plate at $\theta = 40^o$, $z = -23$, 3 and 23*mm*. Dots on the raw images appear skewed and varying in size due to the 40^o imaging angle. Dot-to-dot distances also varied between the three images due to the different z positions. The center column of Fig. 6 shows the corresponding reconstructed images. It is evident that the reconstruction homogenized the dots' sizes across all images, except at the left/right edges where they were too far off the nominal focal plane to be sharply refocused (e.g., right edge of the $z = 23mm$ image and the left edge of $z = -23mm$ were $\pm 48mm$ off-nominal, compared to the system's approx. $\pm$ 25*mm* maximum refocus z-range, as estimated based on [46]). In addition to obtaining well-focused dots, the reconstruction also de-warped the dots into square grid patterns that are well-aligned between images. Portions of the dot-plate outside of the camera's original view remained missing in the reconstructed images.

Quantitative assessment of the reconstruction accuracy was performed by determining the reconstructed dots' coordinates, and comparing them to true dot-plate coordinates. The i^{th} dot's magnitude of spatial error ($e_{mag,i}$) is defined as a combination of the in-plane errors with respect to ground-truths, divided by the image's diagonal dimension:

$$e_{mag,i} = \frac{e_{Euclidean}}{\sqrt{w^2 + h^2}} \times 100\% \tag{1}$$

$$e_{Euclidean} = \sqrt{(x_{true} - x_{recon})^2 + (y_{true} - y_{recon})^2} \tag{2}$$

where, x_{recon} is the detected dot's center coordinate and x_{true} is the ground-truth.

The right of Fig. 6 shows the distributions of $e_{mag,i}$ in the reconstructed images. We observed that $e_{mag,i}$ generally increased towards the corners of the image, perhaps due to a combination of lens distortion and vignette around the corners. From the data in Fig. 6, the image-wide mean e_{mag} can be calculated. Dependence of mean e_{mag} values on dot-plate position and angle are shown in Fig. 7 for all test cases. It is evident that e_{mag} increased with distance from the nominal focal-plane and with angle relative to the optical-axis. Notably, for off-angle cases e_{mag} implicitly includes depth reconstruction error due to the tilt of the dot-plate. In all cases, the magnitudes of error remained well within 1% of the image diagonal dimension.

Table 1. Test cases for the assessment of reconstruction accuracy.

Camera:	4MP	9MP	9MP
Microlens array:	Rect	Rect	Hexa
Sensor *w* (*mm*)	25.6	27.6	27.6
Sensor *h* (*mm*)	16	15.5	15.5
w resolution (*px*)	2560	4096	4096
h resolution (*px*)	1600	2304	2304
px pitch (μm)	10	6.75	6.75
px-per-microlens	12.5	18.5	11.4
Final image *w* (*px*)	205	221	359
Final image *h* (*px*)	128	124	202

Rect: rectangular lens packing, $f = 0.5mm$, f/4, $p_m = 0.125mm$.
Hexa: hexagonal lens packing, 100% fill factor, $f = 0.308mm$, f/4, $p_m = 0.077mm$.

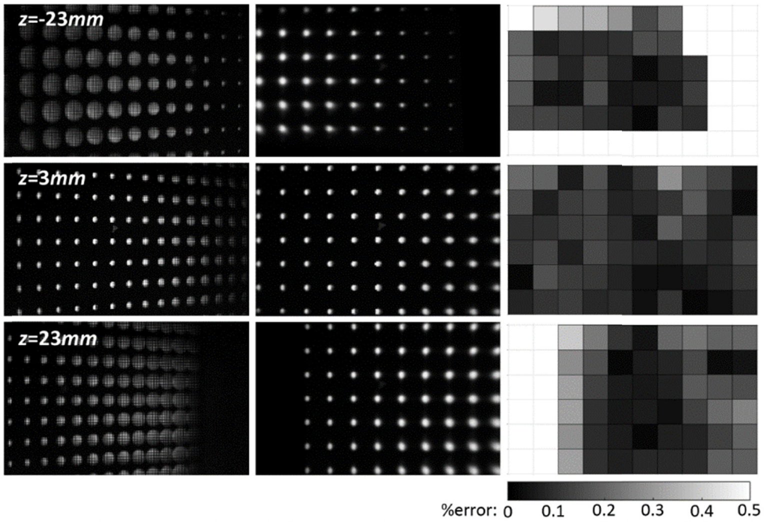

Fig. 6. Comparison of raw plenoptic images at the $z = -23, 3, 23mm$, $\theta = 40^o$ planes (*left*) with their refocused and de-warped counterparts (*center*), and the distributions of % error magnitudes across the images (*right*). Errors in regions without dots cannot be characterized.

From Fig. 7, microlens pitch and pixel-resolution were observed to have no systematic effect upon reconstruction accuracy. However, as Fig. 8 shows, varying microlens pitch had a pronounced effect on the final image's resolution. In both rectangular array cases the dots appeared as featureless and slightly blurred circles. However, for the hexagonal case, the thin inner rim of the drilled metal plate was resolvable, as indicated by the arrows. In plenoptic reconstruction, regions near the nominal focal plane have the worst resolution due to non-uniform ray-sampling at different depths. These resolution degradations are circled in Fig. 8, where the dots appear suddenly pixelated. In the case of the hexagonal microlens array, the pixilation was pronouncedly smoother than the rectangular cases. Differences between the rectangular and hexagonal cases' resolutions are due to plenoptic camera's refocusing physics, where one microlens nominally generates one pixel in the final image [6]; hence, smaller microlenses pack more microlens/final pixel count within the same image area. The 4MP and 9MP cases using the same rectangular lens did not show systematic differences in accuracy or resolution within the tested range. Notably, the Rect and Hexa microlens arrays were optimized for cameras in the range of 5-10MP. Simulations have demonstrated the ability to perform tomographic reconstruction of particle-fields with microlenses having the smaller pitch of 5-8*px*-per-microlens (albeit at reduced maximum refocus *z*-range), which would be better optimized for higher-speed, lower-resolution cameras.

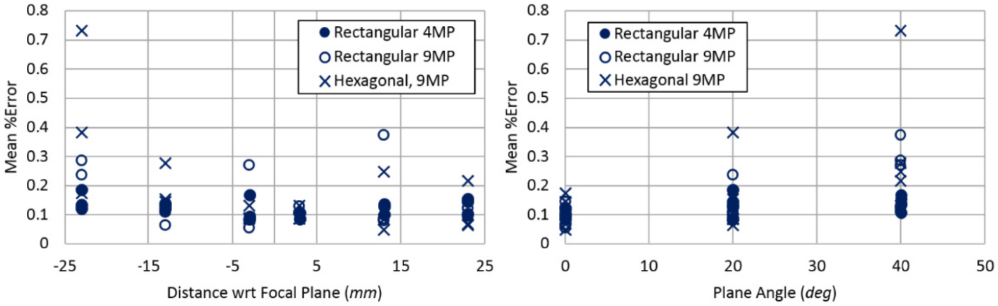

Fig. 7. Variation of mean spatial-errors as a function of plane location and angle.

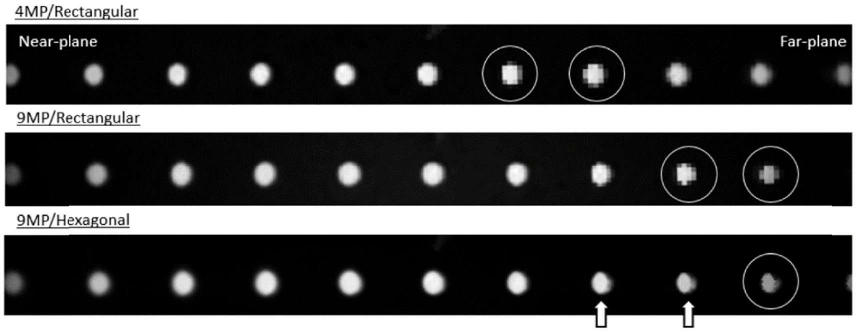

Fig. 8. Comparison of image resolution between the 4MP/Rectangular, 9MP/Rectangular and 9MP/Hexagonal cases. All three Figs. show the de-warped images of dot-plates at the nominal focal-plane, at 20^o relative to the optical axis. Arrows: observable plate rims. Circles: plane of worst resolution.

3.3 Test 3: refocusing and perspective-shift of a high-speed video

To demonstrate post-capture refocusing and perspective-shift, the MPA was used to film: (i) a high-speed scene of falling/bouncing metal ball-bearings and (ii) a dark-room scene through an intensifier. Both scene were filmed with an objective lens magnification of $M \approx 0.5$, which equated to a horizontal field-of-view (FOV) of 35.8 and 55.2*mm*, respectively, at the nominal focal-plane, a nominal depth-of-field (DOF) of 4.5*mm* and extended plenoptic DOF (i.e., extent of depth that can be refocused [46]) of 41*mm*.

Figure 9 shows a sequence of the ball-bearing video captured at 1000*fps* that has been refocused to the objective lens' nominal focal-plane. Progression of the falling ball-bearings can be tracked from frame to frame. Ball-bearings that bounced out of the focal-plane towards the camera became significantly blurred. To show the effect of focal blur, a metal ruler was also placed in the background of Fig. 9, facing diagonally away from the camera. The "4" marking on the ruler is in-focus in this sequence, as shown by the inset, while the "3" marking is blurred as the ruler extended towards the far background.

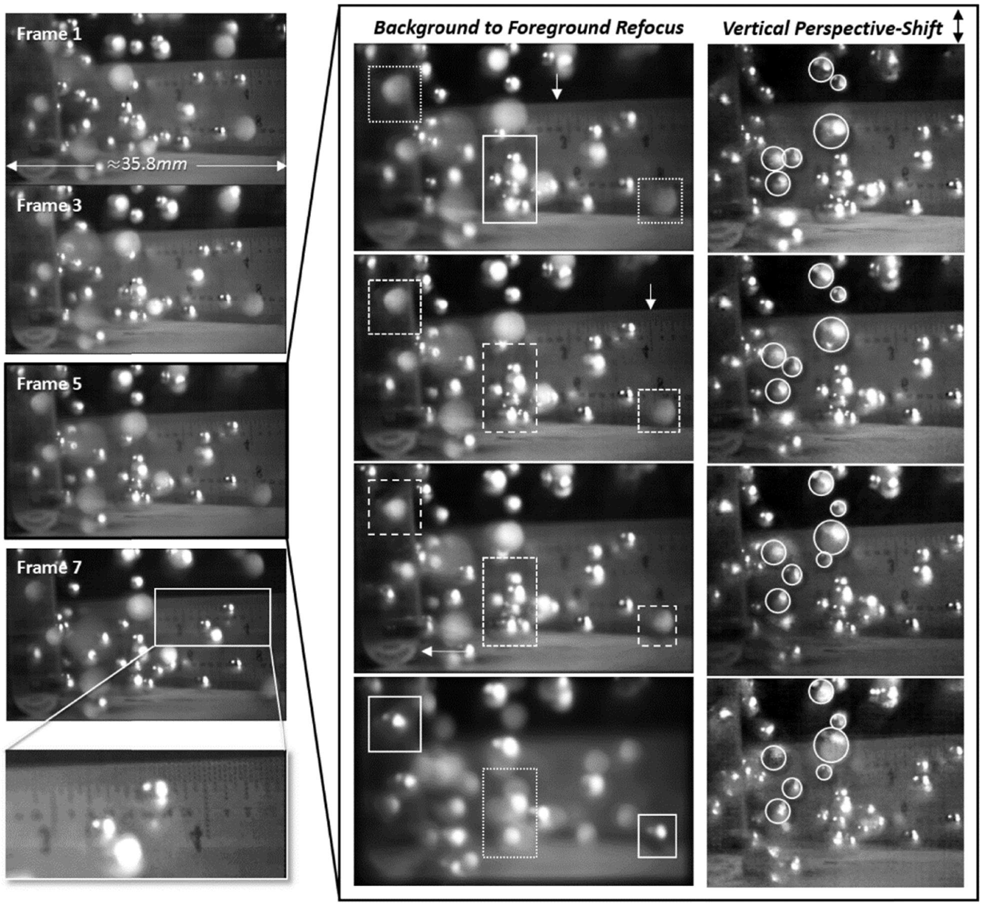

Fig. 9. *Left*: a sequence from 1000*Hz* plenoptic video of free-falling ball-bearings, focused on the nominal focal-plane. *Middle*: refocusing of Frame 5 from background to foreground. (*Arrows*: area of rulers in focus. *Solid boxes*: examples of subjects in focus. *Dotted boxes:* subjects out-of-focus.) *Right*: vertical perspective-shifts. (*Outlines*: examples of subjects that shifted relative to each other between perspectives.)

To demonstrate plenoptic refocusing, the center column of Fig. 9 shows Frame 5 being incrementally refocused from the background to the nominal focal-plane, and then to the foreground. Portions of the ruler that are in focus are marked by arrows, while ball-bearings that are in focus are highlighted by solid boxes. Dashed/dotted boxes show ball-bearings that are currently out-of-focus. In complement, the plenoptic camera's perspective-shift capability is demonstrated on the right column of Fig. 9, where the same frames are viewed from different perspectives along a vertical path. Circles outline the clusters of ball-bearings whose members can be observed to move relative to each other during perspective-shift due to their different depth locations. In certain clusters, members that are completely occluded in one perspective became visible in a different perspective. Notably, Fig. 9 only serves to demonstrate the developed system's refocusing/perspective-shift capability, and tomographic reconstruction of large, optically opaque objects is not possible with a single camera. Instead, 3D triangulation of opaque macro-objects is possible with a non-tomographic Lagrangian approach, as described in [12,47].

Figure 10 shows a photo of the intensified, high-speed plenoptic-imaging system. As previously described, the raw plenoptic image with its dense array of microlens sub-images has to be faithfully captured by the intensifier. Intensifier resolution is thus a critical limiting factor within such a system. The setup in Fig. 10 was installed with the large-pitch Rect microlens (see Table 1) in order to best match available intensifier resolutions- in this case the 69*lp/mm* Lambert Instrument HiCATT, which best matched our Vision Research VEO4k 9MP camera system (~75*lp/mm* equivalent resolution). Despite a loss of resolution, Fig. 10 demonstrates that refocusing is possible on an intensified plenoptic image of a scene containing static objects in a darkened room. For contrast, a non-intensified image of the same scene with identical camera settings is shown. No details could be observed in the non-intensified image.

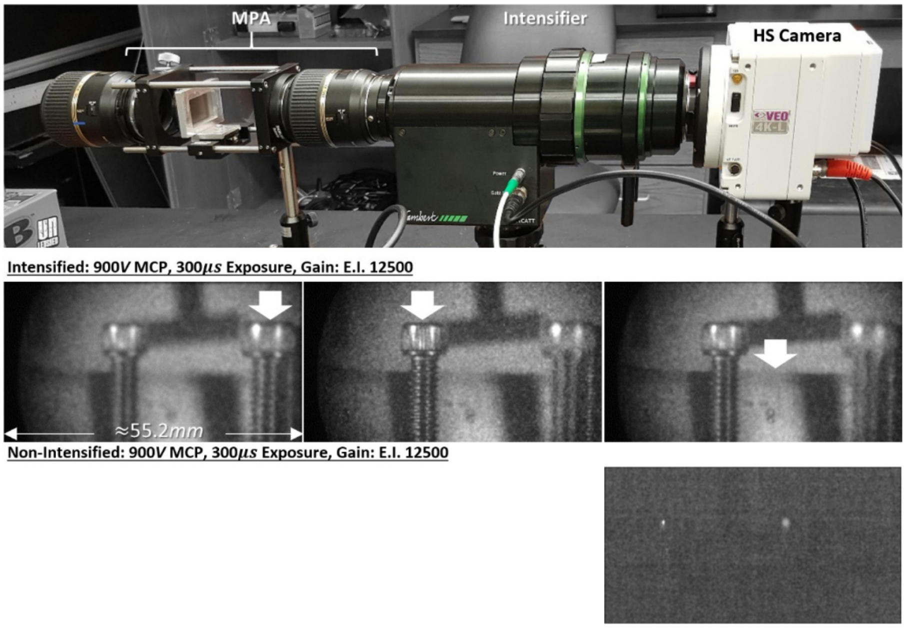

Fig. 10. *Top*: photo of the intensified high-speed plenoptic-imaging system. *Middle row*: an intensified image refocused to different depths (see arrow). *Bottom*: the identically-lit scene imaged without an intensifier.

3.4 Test 4: time-resolved particles-field reconstruction and PPIV

To demonstrate the MPA/high-speed camera system's capability at capturing and reconstructing a 3D particle-field (such as those found in PPIV/tomo-PIV experiments), the system was used to film the plume of droplets emitted by a hand-held sprayer. The left of Fig. 11 shows a sequence of droplets images that were refocused at the nominal focal plane. A constellation of droplets have been highlighted. The sprayer was aimed from left-to-right and away from the camera in this experiment; hence, as the frames unfold the constellation can be observed to travel in a rightward and downward direction, while members of the constellation faded in/out of focus.

The Multiplicative Algebraic Reconstruction Technique (a variant of numerous tomographic reconstruction algorithms [9,29]) was used to reconstruction the droplets-containing volume from the plenoptic images. The resulting volume spanned 50 × 32 × 50*mm* (301 × 193 × 301*vx*). Iso-surface contours of the resulting 3D droplets-field are rendered in the middle and right columns of Fig. 11. The presence of identical constellations on the raw images and *xy* projection of the volume suggests that the reconstruction was qualitatively accurate. Quantitative assessment of the reconstruction accuracy awaits further testing using simulated particles of known positions.

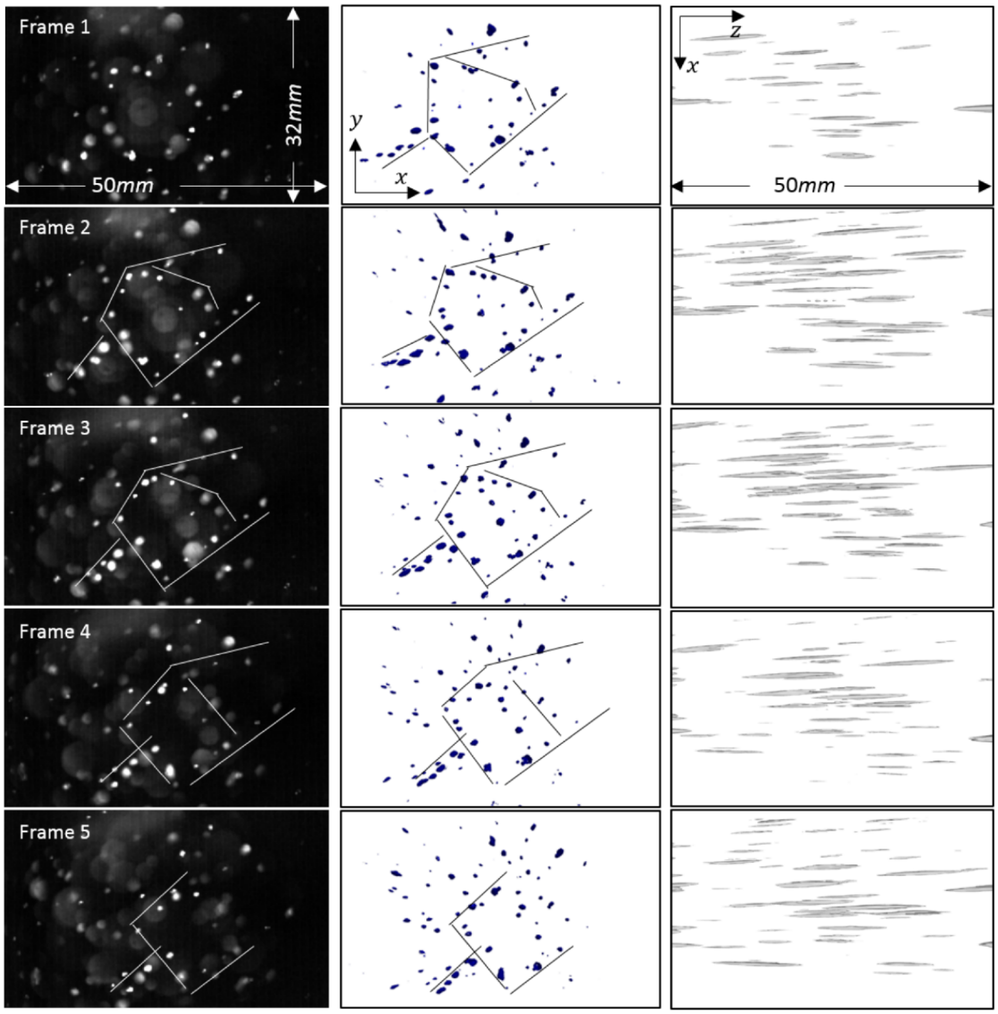

Fig. 11. Reconstruction of a droplets-field from high-speed footage. Common constellations of droplets between the refocused footage (*left*) and the reconstruction's *xy*-view (*center*) are outlined. R*ight*: top-down *xz*-view of the droplets-field.

The right of Fig. 11 exhibits top-down (*x-z*) views of the volume, showing significantly elongation of the otherwise near-spherical droplets in reconstruction. Elongation of objects in reconstruction is chiefly due to the limited parallax baseline of a single plenoptic camera (i.e., large depth ambiguity), which was worsened by having relatively large droplets instead of the micro-particles found in typical PIV experiments. Work by Fahringer & Thurow [11] had reported dramatic reduction in elongation with the addition of just one additional plenoptic camera, while Hall et al. [12] showed that perspective-shifted views from plenoptic images can be used to precisely locate the centers of particles. Future flow tomography using the high-speed system will explore both methods to reduce the effect of elongation.

A standard cross-correlation 3D-PIV was performed on the volumes in Fig. 11, using the standard procedure of 2 passes (window sizes = 128, 64*vx*) with 50% overlaps. A sample of the PIV results is shown in Fig. 12: droplets from the first frame are shown in light gray, while droplets from the second frame are superimposed in black. Streamlines of the calculated velocity-field are initiated along the center plane of the volume. The top plot in Fig. 12 shows that the rightward and downward travel directions of droplets (as observed from Fig. 11) are faithfully captured by the PIV algorithm. Corresponding pairs of droplets between the first and second frames can be seen to lie along the same streamlines. Additionally, the bottom plot in Fig. 12 shows that the component of droplet velocities pointed away-from-camera (+ 've *z*) has also been qualitatively captured by the PIV algorithm. Since the ground-truth velocities of the droplets are not known in this test, the quantitative correctness of the velocity-field is not assessed at this stage.

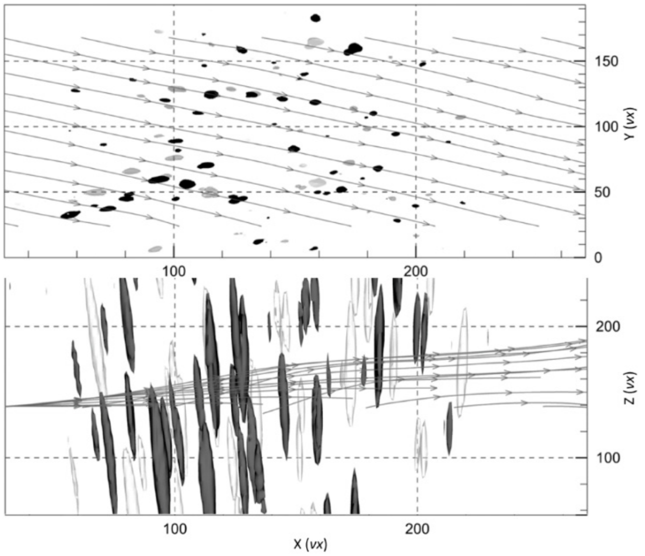

Fig. 12. Streamlines of the velocity-field calculated from frames 1 and 2 of Fig. 11. *Light particles*: droplet at *t*. *Dark particles*: droplets at *t + 1*.

4. Conclusion

A Modular Plenoptic Adaptor (MPA) device was developed for rapid and reversible conversion of high-speed cameras into plenoptic imaging systems capable of $\geq 1kHz$ frame-rate. The device consisted of a main lens, a microlens array and a relay lens mounted on the same optical axis, the collective group of which is attached to a high-speed camera via standard F-mount. This final layout was developed with the cost and physical characteristics of high-speed cameras, as well as the needs of 3D flow-measurements as design constraints (e.g., the need to rapidly convert between 2D/3D imaging without risking sensor-damage, and the need to add an image intensifier between the microlens array and camera sensor).

Four proof-of-concept tests validated the MPA's performance: (i) the relayed plenoptic image was shown to contain negligible distortion, albeit having significant vignette, (ii) volumes reconstructed from the plenoptic images was shown to have <1% spatial error, (iii) two scenes with and without intensifier were successfully filmed and refocused/perspective-shifted post-capture, and (iv) MART tomographic reconstruction and PPIV were performed on a volume of flowing spray droplets with qualitative correct results. Issues identified during the MPA development include: (i) vignette along the image's edge, which can be mitigated by having a larger aperture relay lens or a field-lens/diffuser. (ii) Particle elongation in reconstruction, which was also prevalent in traditional plenoptic camera, and was proven solvable by using an additional plenoptic camera during data acquisition.

In culmination, this study demonstrated one of the first examples of high-speed, intensified light-field imaging, and the first case of time-resolved 3D flow measurement using a plenoptic camera. Furthermore, the study demonstrated a low-cost relayed-plenoptic technique for achieving high-speed light-field imaging without irreversible modifications to the high-speed camera. The modular nature of this concept allows it to be easily adaptable to other camera types (e.g., 10*kHz* high-speed camera, UV-capable intensified camera etc.). The immediate future work will focus on deploying the system to measure canonical 3D flow-fields of known solutions to quantify the system's PPIV accuracy.

Funding

Development of the modular, high-speed plenoptic system was carried out under the National Science Foundation's Major Research Instrumentation Program grant No. 1725929.

References

1. I. Ihrke, J. Restrepo, and L. Mignard-Debise, "Principles of light field imaging: briefly revisiting 25 years of research," IEEE Signal Process. Mag. **33**(5), 59–69 (2016).
2. R. Ng, M. Levoy, M. Bredif, G. Duval, M. Horowitz, and P. Hanrahan, "Light field photography with a hand-held plenoptic camera," Stanford Tech Report CTSR, 1–11 (2005).
3. T.-C. Wang, A. A. Efros, and R. Ramamoorthi, "Occlusion-aware depth estimation using light-field cameras," in the Proceedings of the IEEE International Conference on Computer Vision (IEEE, 2015), pp. 3487–3495.
4. L. Labios, "4D camera could improve robot vision, virtual reality and self-driving cars" (UC San Diego News Center, 2017) *https://ucsdnews.ucsd.edu/pressrelease/4d_camera_could_improve_robot_vision_virtual_reality_and_self_driving_cars*.
5. G. M. Schuster, I. P. Agurok, J. E. Ford, D. G. Dansereau, and G. Wetzstein, "Panoramic Monocentric Light Field Camera," in Proceedings of the International Optical Design Conference (2017), pp. 1–2.
6. K. P. Lynch, *Development of a 3-D Fluid Velocimetry Technique Based On Light Field Imaging* (Auburn University, 2011).
7. T. W. Fahringer and B. S. Thurow, "Tomographic reconstruction of a 3-D flow field using a plenoptic camera," in Proceedings of the 42nd AIAA Fluid Dynamics Conference and Exhibit (AIAA, 2012), pp. 1–13.
8. T. W. Fahringer and B. S. Thurow, "On the development of filtered refocusing: a volumetric reconstruction algorithm for plenoptic-PIV," in Proceedings of the 11th International Symposium on Particle Image Velocimetry (2015), pp. 1–11.
9. T. W. Fahringer, K. P. Lynch, and B. S. Thurow, "Volumetric particle image velocimetry with a single plenoptic camera," Meas. Sci. Technol. **26**(11), 115201 (2015).
10. K. C. Johnson, B. S. Thurow, T. Kim, G. Blois, and K. T. Christensen, "Three dimensional plenoptic PIV measurements of a turbulent boundary layer overlying rough and permeable surfaces," presented at the 18th International Symposium on the Application of Laser and Imaging Techniques to Fluid Mechanics, Lisbon, Portugal, 4–7 July 2016.
11. T. W. Fahringer and B. S. Thurow, "Plenoptic particle image velocimetry with multiple plenoptic cameras," Meas. Sci. Technol. **29**(7), 075202 (2018).
12. E. M. Hall, D. R. Guildenbecher, and B. S. Thurow, "3D particle location from perspective-shifted plenoptic images," presented at the 19th International Symposium on the Application of Laser and Imaging Techniques to Fluid Mechanics, Lisbon, Portugal, 16–19 July 2018.
13. A. Bichal, *Development of 3D Background Oriented Schlieren with a Plenoptic Camera* (Auburn University, 2015).
14. J. N. Klemkowsky, B. S. Thurow, and R. Mejia-Alvarez, "3D visualization of density gradients using a plenoptic camera and background oriented schlieren imaging," in Proceedings of the AIAA SciTech Forum and Exposition (AIAA, 2016), pp. 1–12.
15. J. N. Klemkowsky, T. W. Fahringer, C. J. Clifford, B. F. Bathel, and B. S. Thurow, "Plenoptic background oriented schlieren imaging," Meas. Sci. Technol. **28**(9), 095404 (2017).
16. J. Sun, M. M. Hossain, C. Xu, and B. Zhang, "Investigation of flame radiation sampling and temperature measurement through light field cameras," Int. J. of Heat Mass Transf. **121**, 1281–1296 (2018).
17. X. Huang, H. Qi, X.-L. Zhang, Y.-T. Ren, L.-M. Ruan, and H.-P. Tan, "Application of Landweber method for three-dimensional temperature field reconstruction based on the light-field imaging technique," J. Heat Transfer **140**(8), 082701 (2018).
18. A. Fischer, C. Kupsch, J. Gürtler, and J. Czarske, "High-speed light field camera and frequency division multiplexing for fast multi-plane velocity measurements," Opt. Express **23**(19), 24910–24922 (2015).
19. Y. Ishino and N. Ohiwa, "Three-dimensional computerized tomographic reconstruction of instantaneous distribution of chemiluminescence of a turbulent premixed flame," JSME Int. J. **48**(1), 34–40 (2005).
20. J. Floyd, P. Geipel, and A. M. Kempf, "Computed tomography of chemiluminescence (CTC): instantaneous 3D measurements and phantom studies of a turbulent opposed jet flame," Combust. Flame **158**(2), 376–391 (2011).
21. W. Cai, X. Li, F. Li, and L. Ma, "Numerical and experimental validation of a three-dimensional combustion diagnostic based on tomographic chemiluminescence," Opt. Express **21**(6), 7050–7064 (2013).
22. X. Li and L. Ma, "Capabilities and limitations of 3D flame measurements based on computed tomography of chemiluminescence," Combust. Flame **162**(3), 642–651 (2015).
23. J. Sakakibara and R. J. Adrian, "Whole field measurement of temperature in water using two-color laser induced fluorescence," Exp. Fluids **26**(1–2), 7–15 (1999).

24. S. Deusch and T. Dracos, “Time resolved 3D passive scalar concentration-field imaging by laser induced fluorescence (LIF) in moving liquids,” Meas. Sci. Technol. **12**(2), 188–200 (2001).
25. J. P. Crimaldi, “Planar laser induced fluorescence in aqueous flows,” Exp. Fluids **44**(6), 851–863 (2008).
26. Y. Wu, W. Xu, Q. Lei, and L. Ma, “Single-shot volumetric laser induced fluorescence (VLIF) measurements in turbulent flows seeded with iodine,” Opt. Express **23**(26), 33408–33418 (2015).
27. L. Ma, Q. Lei, T. Capil, S. D. Hammack, and C. D. Carter, “Direct comparison of two-dimensional and three-dimensional laser-induced fluorescence measurements on highly turbulent flames,” Opt. Lett. **42**(2), 267–270 (2017).
28. E. Goldhahn and J. Seume, “The background oriented schlieren technique: sensitivity, accuracy, resolution and application to a three-dimensional density field,” Exp. Fluids **43**(2–3), 241–249 (2007).
29. F. Scarano, “Tomographic PIV: principles and practice,” Meas. Sci. Technol. **24**(1), 012001 (2013).
30. G. E. Elsinga, F. Scarano, B. Wieneke, and B. W. van Oudheusden, “Tomographic particle image velocimetry,” Exp. Fluids **41**(6), 933–947 (2006).
31. B. Coriton, A. M. Steinberg, and J. H. Frank, “High-speed tomographic PIV and OH PLIF measurements in turbulent reactive flows,” Exp. Fluids **55**(6), 1743 (2014).
32. C. Brücker, D. Hess, and J. Kitzhofer, “Single-view volumetric PIV via high-resolution scanning, isotropic voxel restructuring and 3D least-squares matching (3D-LSM),” Meas. Sci. Technol. **24**(2), 024001 (2013).
33. H. Meng, G. Pan, Y. Pu, and S. H. Woodward, “Holographic particle image velocimetry: from film to digital recording,” Meas. Sci. Technol. **15**(4), 673–685 (2004).
34. A. A. Aguirre-Pablo, A. B. Aljedaani, J. Xiong, R. Idoughi, W. Heidrich, and S. T. Thoroddsen, “Single-camera 3D PTV using particle intensities and structured light,” Exp. Fluids **60**(2), 25 (2019).
35. E. Kristensson, Z. Li, E. Berrocal, M. Richter, and M. Alden, “Instantaneous 3D imaging of flame species using coded laser illumination,” Proc. Combust. Inst. **36**(3), 4585–4591 (2017).
36. B. R. Halls, P. S. Hsu, S. Roy, T. R. Meyer, and J. R. Gord, “Two-color volumetric laser-induced fluorescence for 3D OH and temperature fields in turbulent reacting flows,” Opt. Lett. **43**(12), 2961–2964 (2018).
37. T. R. Meyer, B. R. Halls, N. Jiang, M. N. Slipchenko, S. Roy, and J. R. Gord, “High-speed, three-dimensional tomographic laser-induced incandescence imaging of soot volume fraction in turbulent flames,” Opt. Express **24**(26), 29547–29555 (2016).
38. E. H. Adelson and J. Y. A. Wang, “Single lens stereo with a plenoptic camera,” IEEE Trans. Pattern Anal. Mach. Intell. **14**(2), 99–106 (1992).
39. M. Levoy and P. Hanrahan, “Light field rendering,” in Proceedings of the 23rd Annual Conference on Computer Graphics and Interactive Techniques (1996), pp. 31–42.
40. M. Levoy, “Light fields and computational imaging,” Computer **39**(8), 46–55 (2006).
41. A. Lumsdaine and T. Georgiev, “The focused plenoptic camera,” in Proceedings of the IEEE International Conference on Computational Photography (IEEE, 2009), pp. 1–8.
42. G. Wu, B. Masia, A. Jarabo, Y. Zhang, L. Wang, Q. Dai, T. Chai, and Y. Liu, “Light field image processing: an overview,” IEEE J. Sel. Top. Signal Process. **11**(7), 926 (2017).
43. V. Drazic, J.-J. Sacre, A. Schubert, J. Bertrand, and E. Blonde, “Optimal design and critical analysis of a high-resolution video plenoptic demonstrator,” J. Electron. Imaging **21**(1), 011007 (2012).
44. Y. Liu, M. M. Hossain, J. Sun, C. Xu, B. Zhang, and S. Wang, “Design a cage-typed light field camera system for flame measurement,” in Proceedings of IEEE Sensors (IEEE, 2017), pp. 1–4.
45. E. M. Hall, T. W. Fahringer, D. R. Guildenbecher, and B. S. Thurow, “Volumetric calibration of a plenoptic camera,” Appl. Opt. **57**(4), 914–923 (2018).
46. T. W. Fahringer and B. S. Thurow, “The effect of microlens size on the performance of single-camera plenoptic PIV,” presented at the 19th International Symposium on the Application of Laser and Imaging Techniques to Fluid Mechanics, Lisbon, Portugal, 16–19 July 2018.
47. E. M. Hall, D. R. Guildenbecher, and B. S. Thurow, “Development and uncertainty characterization of 3D particle location from perspective shifted plenoptic images,” Opt. Express **27**(6), 7997–8010 (2019).